

Simple and versatile heterodyne whole-field interferometer for phase optics characterization

D. M. Silva, E. A. Barbosa, and N. U. Wetter

Citation: *Rev. Sci. Instrum.* **83**, 103103 (2012); doi: 10.1063/1.4757396

View online: <http://dx.doi.org/10.1063/1.4757396>

View Table of Contents: <http://rsi.aip.org/resource/1/RSINAK/v83/i10>

Published by the [American Institute of Physics](#).

Related Articles

Continuously tunable optical multidimensional Fourier-transform spectrometer

Rev. Sci. Instrum. **84**, 023107 (2013)

The frequency stabilization method of laser feedback interferometer based on external cavity modulation

Rev. Sci. Instrum. **84**, 025108 (2013)

Efficient end-fire coupling of surface plasmons on flat metal surfaces for improved plasmonic Mach-Zehnder interferometer

J. Appl. Phys. **113**, 053101 (2013)

Automation of an “Aculight” continuous-wave optical parametric oscillator

Rev. Sci. Instrum. **84**, 013102 (2013)

Two-path solid-state interferometry using ultra-subwavelength two-dimensional plasmonic waves

Appl. Phys. Lett. **102**, 021104 (2013)

Additional information on *Rev. Sci. Instrum.*

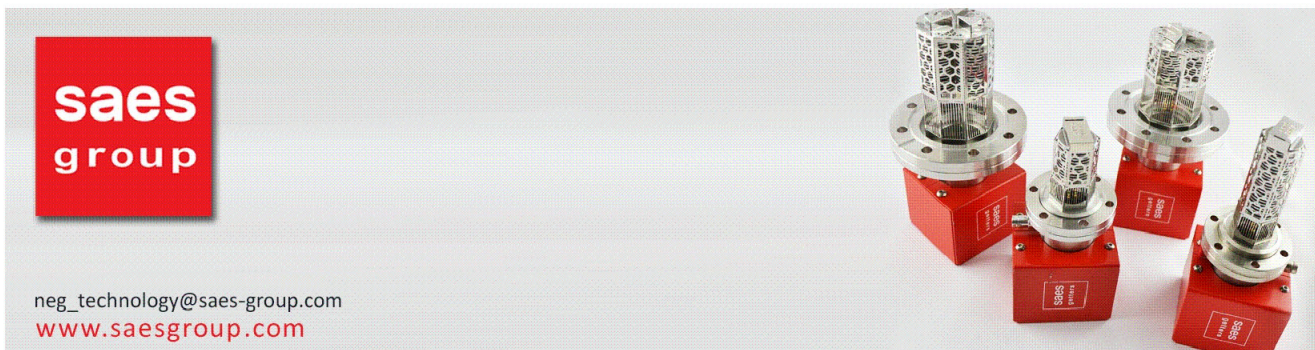
Journal Homepage: <http://rsi.aip.org>

Journal Information: http://rsi.aip.org/about/about_the_journal

Top downloads: http://rsi.aip.org/features/most_downloaded

Information for Authors: <http://rsi.aip.org/authors>

ADVERTISEMENT



The advertisement features the Saes Group logo on the left, which consists of the word "saes" in white lowercase letters above the word "group" in white lowercase letters, both on a red square background. To the right of the logo is a photograph of four precision optical instruments. Each instrument has a red base with the Saes Group logo and a silver-colored metal top section with a complex, perforated cylindrical structure. The instruments are arranged in a cluster, with one in the foreground and three behind it.

neg_technology@saes-group.com
www.saesgroup.com

Simple and versatile heterodyne whole-field interferometer for phase optics characterization

D. M. Silva,¹ E. A. Barbosa,^{2,a)} and N. U. Wetter¹

¹*Instituto de Pesquisas Energéticas e Nucleares (CNEN-IPEN/SP), CEP 005508-000 São Paulo, Brazil*

²*Laboratório de Óptica Aplicada, Faculdade de Tecnologia de São Paulo, CEETEPS-UNESP, Pça Cel Fernando Prestes, 30, CEP 01124 060, São Paulo, Brazil*

(Received 14 June 2012; accepted 18 September 2012; published online 5 October 2012)

A wavefront sensor for thermally induced lens and passive lens characterization based on low-coherence digital speckle interferometry was developed and studied. By illuminating the optical setup with two slightly detuned red diode lasers, whole-field contour interference fringes were generated according to the resulting synthetic wavelength. For fringe pattern visualization the optical setup used the light transmitted through a ground glass plate as object beam. The performance of the sensor was investigated and its versatility was demonstrated by measuring the thermal lens induced in an Er-doped glass sample pumped by a 1.76-W diode laser emitting at 976 nm and by evaluating the wavefront distortion introduced by an ophthalmic progressive lens. © 2012 American Institute of Physics. [<http://dx.doi.org/10.1063/1.4757396>]

I. INTRODUCTION

Wavefront sensing comprises a group of methods through which the spatial phase distribution of an electromagnetic wave is determined. This measurement finds several applications in fields such as profilometry, ophthalmology, quality control in optical manufacturing and astronomy, among many others.¹ By determining the wavefront shape, information on the studied phenomena or the measured optical component can be retrieved. The different techniques that are employed for the characterization of phase optical components can be basically divided into three groups, namely, methods based on geometrical optics such as Shack-Hartmann (SH), speckle-related methods using random phase diffusers (RPD), and interferometric systems.

The SH aberrometer was developed in the early 1970s and is the most widely and successfully employed device in fields such as atmospheric turbulence detection and correction by adaptive optics for astronomy, aberration measurement of the human eye in ophthalmology and quality control of lens fabrication, among others.² The SH sensing principle consists in passing the wavefront through a microlens array. By measuring the displacements suffered by the spots focused onto a CCD sensor the form of the wavefront can be determined. The most remarkable characteristics of the SH device is its simplicity, robustness, and compactness. Moreover, the SH is known to be moderately vibration immune and wavelength independent due to its geometrical optics character. The combination of all those characteristics allowed for the development and construction of several commercial SH wavefront sensors for applications in real-life environments.

Random phase diffusers generate speckle patterns from the original incident wave in a stochastic way.^{3,4} By properly translating this component to the aperture plane, the speckle patterns are used to reconstruct the wavefront by applying an iterative phase retrieval algorithm. Differently from the

SH aberrometers, whose spatial resolution is limited by the distance between the microlenses (typically 100 μm), this speckle technique achieves spatial resolutions in the order of 10 μm , imposed by the diffuser properties.⁵

Whole-field interferometric methods are very well known and established techniques.⁶ With the advent of digital speckle pattern interferometry (DSPI) and holographic interferometry the wavefront reconstruction processes became more sophisticated, accurate, and versatile.⁷⁻¹⁰ By generating contour interferograms, those processes enabled the development of wavefront sensors with high spatial resolution and accuracy. Moreover, interferometric methods allow the construction of wavefront sensors with several setup configurations, each one suitable for a given application. More recently introduced, digital holography can numerically reconstruct the wavefront phase directly from the recorded contour interference pattern generated by the object and the reference waves.^{11,12} This can be carried out provided the wavefront dimensions range within few wavelengths, otherwise the spatial period of the resulting phase map becomes indistinguishable. Indeed, if the wavefront depth far exceeds the wavelength, it is necessary to use auxiliary double exposure procedures in order to get discernible and low-spatial frequency contour fringes and obtain low-noise measurements. Homodyne double-exposure interferometry can be implemented, e.g., by using rotating mirrors¹³ or by taking the difference of retrieved phase maps,¹⁴ while double-exposure heterodyne methods use single tunable laser setups.¹⁵

The present study aims at eliminating or minimizing the limitations of the wavefront sensors described above for material and device characterization through DSPI. In order to overcome the relatively low dynamic range of conventional interferometers a heterodyne two-laser whole-field setup was employed. Both lasers were properly tuned and aligned in order to have the same propagation direction and to be spatially superimposed. The resulting synthetic wavelength ranging from hundreds of micrometers to few millimeters allowed the generation of real-time, single-exposure, easily

^{a)}Electronic mail: ebarbosa@fatecsp.br.

discernible contour fringes. By tuning the lasers the precision and the sensitivity of the measurement could be conveniently scaled. In addition, the spatial resolution of the DSPI setup used in this work far exceeds the resolution of the commercially available Shack-Hartmann devices, since the pixel size of the CCD or CMOS targets used for speckle pattern acquisition is much smaller than the typical size of the microlenses of the SH sensors. Another distinguishing aspect of our DSPI wavefront sensor is the possibility of real-time monitoring of dynamical processes. Unlike the Shack-Hartmann, DSPI and holographic techniques used for lens characterization and reported in the literature, the two-wavelength interferometer developed in this work does enable the visualization of contour fringes in real time. This property makes the device most suitable for the analysis of the thermal lens (TL) evolution in solid state lasers during laser action, as well as the study of induced lensing in transient phenomena.

To the best of our knowledge this is the first demonstration of a heterodyne DSPI device whose versatile geometry does enable the characterization of both phase distorters and induced lenses without significant changes in the optical configuration. The interference fringes describing the wavefront are formed onto a ground glass plate and the wavefront is reconstructed upon fringe evaluation through phase stepping techniques and phase unwrapping procedures. In this work, two different phenomena were studied: the wavefront distortion introduced by an ophthalmic progressive lens and the thermal lensing in an Er-doped CaO–Al₂O₃ glass sample pumped by a 1.8 W diode laser. An expression providing the focal length of the thermally induced lens as a function of the geometrical parameters of the setup and the radius of curvature of the reconstructed wavefront was also derived.

II. TWO-WAVELENGTH DSPI

Let us consider the incidence of two coherent object (S) and reference (R) beams onto the target of a CCD camera. Each beam originates from the superposition of two waves 1 and 2 with lengths λ_1 and λ_2 , respectively, which propagate along the same direction. At the CCD target R and S are given by

$$\begin{aligned} R_N &= R_0 \left(e^{i(k_1 \Gamma_R + \phi_1)} + e^{i(k_2 \Gamma_R + \phi_2)} \right) \\ S_N &= S_0 \left[e^{i(k_1 \Gamma_S(x,y) + \phi_1)} + e^{i(k_2 \Gamma_S(x,y) + \phi_2)} \right], \end{aligned} \quad (1)$$

where $k_{1,2} = 2\pi/\lambda_{1,2}$, ϕ_1 and ϕ_2 are the phases at the output of lasers 1 and 2, respectively, and $\Gamma_S(x, y)$ is the object wave coming from a point (x, y) on the glass plate and Γ_R is the optical path of the reference wave. As usually occurs in DSPI and holography, the reference wave is planar, while the signal wave results from light coming from a diffusely scattering surface, so that the dependence of Γ_S on the spatial coordinates x and y is related to the geometry of the signal wavefront. The resulting interference pattern recorded at the CCD is formed by a high-spatial frequency term due to the randomly distributed speckle pattern and a low-spatial frequency term describing the macroscopic geometry of the signal wavefront related to the difference $\lambda_1 - \lambda_2$. By eliminating the

strong background generated by the reference beam through the subtractive method,¹⁶ the speckle modulated contour interference fringes can be clearly visualized. After low-pass filtering, the contour interferogram signal V is given by⁹

$$V(x, y) = V_0 \cos^2 \left[\frac{\pi}{\lambda_S} (\Gamma_S(x, y) - \Gamma_R) \right], \quad (2)$$

where $V_0 \propto R_0 S_0$ and the quantity $\lambda_S \equiv \lambda_1 \lambda_2 / |\lambda_2 - \lambda_1|$ is known as the synthetic wavelength. Equation (2) was obtained by taking into account the random behavior in time of the phase difference $\phi_1 - \phi_2$ since both lasers are mutually incoherent.¹⁷ The low spatial frequency interferogram formation can be attributed to the moiré-like effect due to the spatial superposition of two similar speckle patterns generated by waves 1 and 2. Due to the typically small difference between λ_1 and λ_2 both patterns present slightly different spatial frequencies; the resulting frequency beating generates the contour interferogram according to λ_S . The term $\Gamma_S(x, y) - \Gamma_R$ in the phase shows that the resulting interferogram describes the scattering surface wavefront modulated by contour interference fringes whose spatial frequency depends both on the surface geometry and the synthetic wavelength. The fringes represent the intersection of the wavefront with parallel, equally spaced planes of constant elevation. The distance between two consecutive planes is the contour interval. The wavelengths must be adjusted in order to enable the best measurement sensitivity, provided the trade-off between interferogram spatial frequency and camera resolution is observed in order to assure a good fringe visibility.

The quantitative evaluation of the fringe pattern provides the wavefront 3D reconstruction. In the literature several fringe evaluation methods are reported, such as continuous phase shifting,¹⁸ phase stepping,¹⁹ and Fourier-transform methods.²⁰ In this work we use the four-stepping technique in which four $\pi/2$ -phase shifted interferograms with respect to the synthetic wavelength are acquired and combined in order to obtain the wavefront phase map. This map in turn is unwrapped through the branch-cut technique²¹ thus providing the reconstructed wavefront.

III. OPTICAL SCHEME OF THE WAVEFRONT SENSOR

Figure 1(a) shows a schematic diagram of the setup used which is a basic configuration for DSPI or digital image plane holography.²² Through beam splitter BS1 both beams originating from tunable diode lasers 1 and 2 are spatially superimposed and propagate along the same direction. The reference beam passes through the spatial filter (SF), is partially reflected by beam splitter BS2 and illuminates the CCD. In the object-beam arm the positive lenses L1 and L2 form a nearly confocal expander and collimate the beam which illuminates the diffusive glass plate. The objective lens L3 builds the image of the plate at the CCD target with the help of mirrors M2 and M3. If the illuminating wave at normal incidence to the diffuser plate is perfectly planar, the resulting contour speckle interferogram presents an infinite spatial period with no contour fringes. Otherwise, the speckle image of the plate presents the contour interferogram describing the impinging

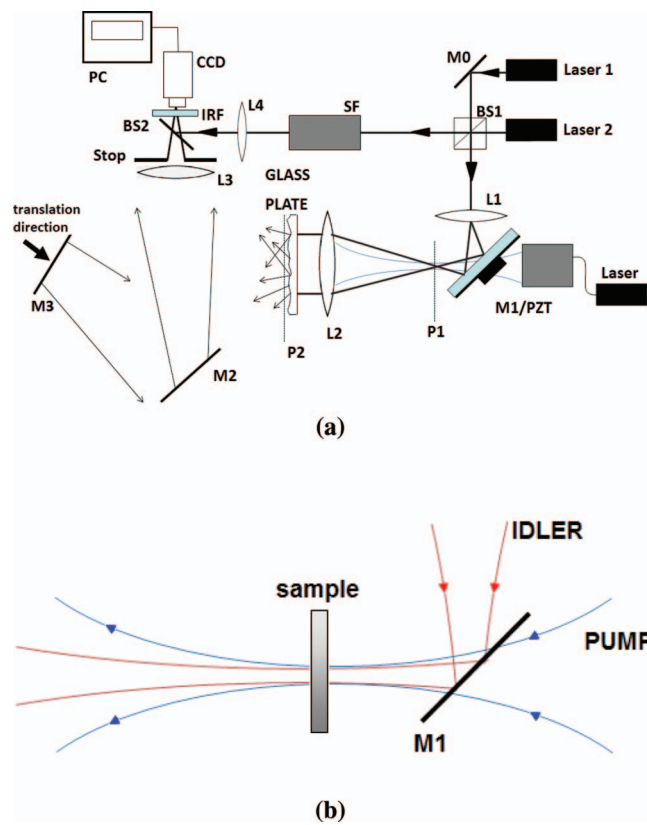


FIG. 1. (a) Optical setup: BS1 and BS2, beam splitters; L1–L4, lenses; M0–M3, mirrors; SF, spatial filter; IRF, infrared filter; CCD, camera; PC, computer. The arrow at mirror M3 shows the direction along which it is translated. (b) Scheme of the idler and the pump beams at the dichroic mirror M1.

wavefront with a contour interval Δz which equals the synthetic wavelength.

The wavefront sensor can detect and measure the wavefront geometry generated by passive elements as well as by induced-lens phenomena. If a passive wavefront distorter such as an ordinary lens is positioned right after the diffusive plate, or if a lens is induced between lenses 1 and 2, the wavefront geometry is changed and consequently the contour interferogram describes the form of the new wavefront generated by the distorter.

A. Thermal and nonlinear lens measurement

Induced lensing in a photonic material is generated by tightly focusing a high-intensity pump beam into it. The lens-like effect is either due to a nonlinear response of the sample, e.g., Kerr lensing²³ or photorefractive lensing,²⁴ or to local absorption followed by thermal lensing or a mixture of both effects. Thermal lensing is a combination of refractive index change with temperature dn/dT , photoelastic effects and end face bulging due to material expansion. The higher the pump intensity, the more enhanced the lensing effect. In the present setup thermal lensing is induced by focusing the pump beam into the sample through mirror M1, as shown in Figure 1(b). Between M1 and lens L2 the object beam originated from the illuminating diode lasers (idler beam) and the pump beam propagate collinearly. By placing the sample under study near

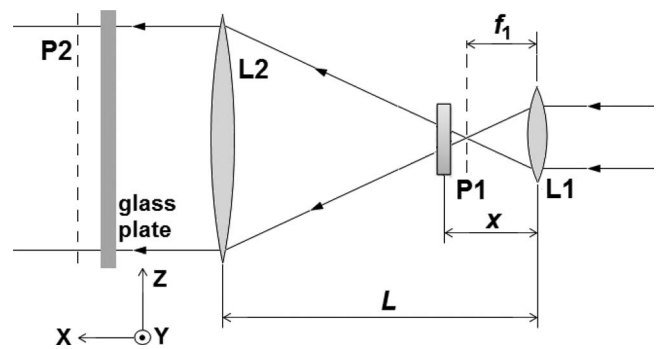


FIG. 2. Optical scheme of the confocal beam expander.

the focal plane P1 of lens L1, the lens induced by the pump changes the wavefront of the idler at the diffusive plate, thus generating low-spatial frequency contour fringes. The dichroic mirror M1 is highly reflective for the idler beam wavelength and highly transmitting at the pump beam wavelength.

It is convenient to determine the equation providing the focal length f of an induced lens TL placed between lenses L1 and L2 as a function of the wavefront geometry and the experimental parameters. A simplified but effective calculation can be carried out through the well-known ABCD matrix formalism considering the transformation experienced by the Gaussian beam parameter $1/q_i = 1/R_i - i\lambda/\pi\omega_i^2$ when the wave impinges lens L1 and propagates to the glass diffuser plate, where R_i is the radius of the wavefront and ω_i is the beam radius at point i . Figure 2 shows the optical scheme of the confocal beam expander (except mirror M1) with lens TL and the distance x between TL and L1 to be determined. The beam parameters q_1 at the input of L1 and q_2 at the output of L2 are related according to²⁵

$$\frac{1}{q_2} = \frac{C + D/q_1}{A + B/q_1}, \quad (3)$$

where A , B , C , and D are the elements of the matrix describing the propagation of the wave through the beam expander. At input plane L1 the incoming wave is approximately planar so that $1/R_1 = 0$; with the help of Eq. (3) the radius R_2 of the wavefront after lens L2 is given by

$$\frac{1}{R_2} = \frac{ACb_1^2 + BD}{A^2b_1^2 + B^2}, \quad (4)$$

where $b_1 \equiv \pi\omega_1^2/\lambda$ is the confocal parameter of the beam at input lens L1. In the experiments, due to the relatively large diameter of this beam, $A^2b_1^2 \gg B^2$ and $ACb_1^2 \gg BD$, so that Eq. (4) reduces to

$$\frac{1}{R_2} \cong \frac{C}{A}. \quad (5)$$

According to the optical scheme of Figure 2, the elements A and C are written by

$$A = \frac{1}{f_{TL}} \left(\frac{x}{f_1} - 1 \right) (L - x) + 1 - \frac{L}{f_1} \quad (6a)$$

$$C = \frac{1}{f_{TL}} \left(\frac{x}{f_1} - 1 \right) \left(1 - \frac{L - x}{f_2} \right) - \frac{1}{f_1} - \frac{1}{f_2} + \frac{L}{f_1 f_2}, \quad (6b)$$

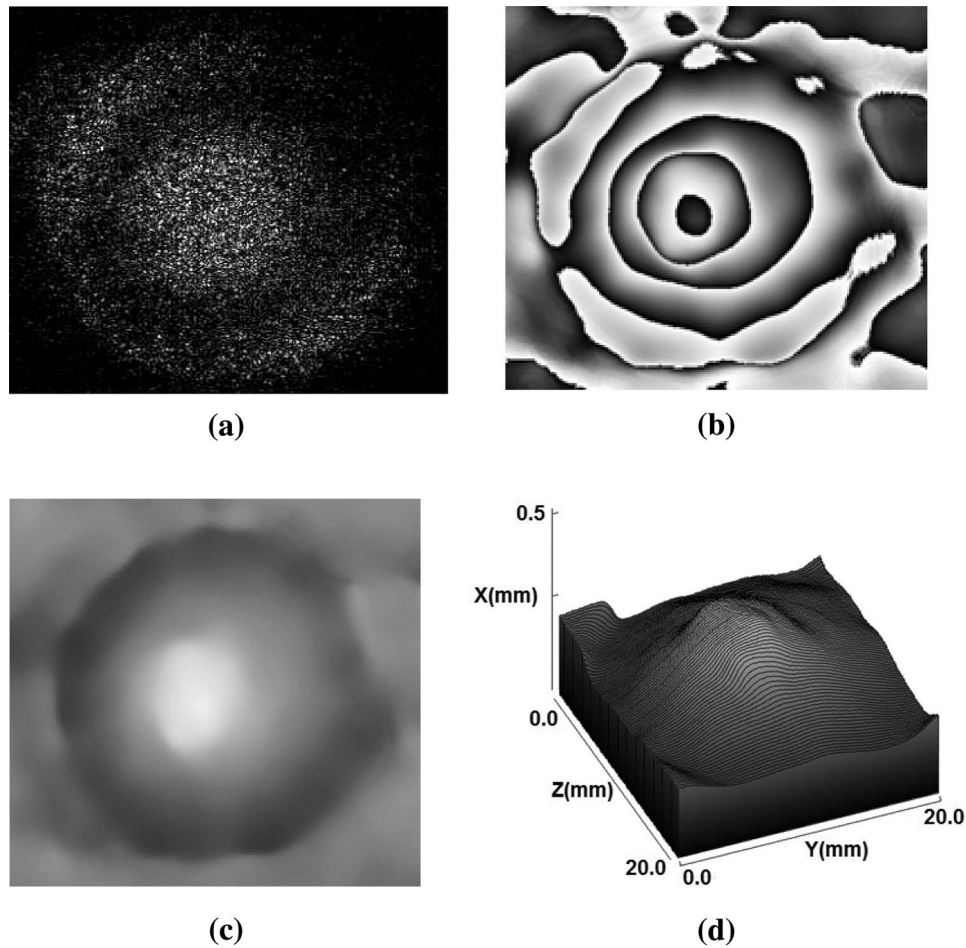


FIG. 3. Wavefront generated by the thermally induced lens: (a) speckle pattern; (b) phase map; (c) unwrapped phase; (d) 3D reconstructed wavefront.

where f_{TL} is the focal length of the induced lens. From Eqs. (5) and (6) f_{TL} becomes

$$f_{TL} = \frac{\left(\frac{x}{f_1} - 1\right) \left[R_2 \left(1 - \frac{L-x}{f_2}\right) - L + x \right]}{1 - \frac{L}{f_1} + \frac{R_2}{F}}, \quad (7)$$

where $F^{-1} \equiv 1/f_1 + 1/f_2 - L/(f_1 f_2)$ is the optical power of the beam expander without thermal lensing. From above Eq. (7) f_{TL} can be experimentally determined by measuring the distance x of the sample to the lens L1 and by determining the radius of curvature R_2 of the reconstructed wavefront.

Equation (5) shows that an incident plane wave can get distorted when passing through an optical system, so that the radius of curvature of the emerging wavefront equals the total dioptric power C/A of the system. By determining the phase of the reconstructed wavefront this radius of curvature can be obtained.

B. Spherical and aspherical lens measurement

The wavefront geometry generated by a lens or other transparent distorter can be evaluated by placing the object at plane P2 after the ground glass plate of the wavefront sensor (see Figure 1). According to Eq. (2) the resulting DSPI image displays the diffusive glass covered with contour interference fringes due to the wavefront deformation caused by

the lens. Those fringes describe the wavefront geometry at the lens output and result from the combination of the distortion caused by the test lens and a residual wavefront deformation related to aberration phenomena in the optical imaging system and eventual alignment errors in the optical setup. This latter effect can be observed and quantitatively evaluated in the absence of the test lens and usually has the form of nearly circular concentric fringes. In a thin-lens approximation, the focal distance f_L of the lens can be obtained as

$$\frac{1}{f_L} \cong \frac{1}{R} - \frac{1}{R'}, \quad (8)$$

where R' is the radius of curvature of the residual wavefront and R is the radius of curvature at the test lens output, both obtained from the reconstructed wavefronts.

IV. EXPERIMENTS AND RESULTS

The emission line of the two 40-mW diode lasers used in the DSPI setup is centered at 650 nm. Upon proper adjustments in the drive currents, the lasers were tuned to 654.12 nm and 657.70 nm, thus, resulting in a contour interval of $120 \pm 1 \mu\text{m}$. Both laser beams were spatially superimposed by beam splitter BS1 upon properly tilting and translating mirror M0, shown in Figure 1. Lens L3 forms the test object image at the CCD target. The CCD camera (Sony

SSC-C104, 768×494 pixels) with pixel size of $\sim 15 \times 15 \mu\text{m}^2$ is connected to a computer for image acquisition and further analysis. The size of the speckle grain was matched to the pixel size to achieve maximum contrast by positioning a stop at the aperture of L3. It is convenient to make the illuminated area of the glass plate sufficiently large to enable an easy visualization of the contour fringes. This was obtained by choosing the focal lengths of lenses L1 and L2 of the telescope to be $f_1 = 25$ mm and $f_2 = 260$ mm, providing an illuminated plate area with 30-mm diameter.

The phase shifts for the four-stepping routine were introduced by a micrometric screw attached to the mount of mirror M3. This mirror was supported by a piezoelectric transducer excited with a ~ 4 -Hz dither signal for phase modulation of the reference beam, as carried out in Ref. 8, in order to enhance the fringe pattern visibility. In this method the first frame is stored, the reference beam is then phase-modulated, and a speckle-decorrelated second frame is obtained.¹⁶

The experiments described below were carried out in order to analyze the sensor performance.

A. Thermal lens measurement

A good superposition of the modes of the idler and the pump beams seems to be an interesting experimental configuration, which suggests the positioning of the sample at plane P1 shown in Figure 1, for which $x = f_1$. However, according to Eq. (6), at this sample position the radius of curvature R_2 does not depend on the thermal lens focal length, regardless of the other experimental parameters, so this configuration is insensitive to induced lensing. Thus, in the experiments the sample must be positioned between lenses L1 and L2 in such a way as to satisfactorily superimpose the idler and the pump modes and at the same time enhance the sensitivity of the wavefront sensor.

The pump source is a fiber-coupled, thermoelectrically cooled diode laser (OptoPower, BF-NSI-ENG) with emission centered at 974 nm and operation temperature of 23 °C. At the fiber output the beam quality factor is $M^2 = 159$ and the beamwaist is 230 μm . The thermal lens was induced in a 4%-Er doped CaO- Al_2O_3 glass sample with dimensions $2.4 \times 6.1 \times 4.1$ ($x \times y \times z$) mm^3 and absorption peak at 976 nm. The pump and the idler beams propagate along the sample's x -direction.

Once the sample is illuminated by the pump laser a very fast, random, and continuous change in the high-spatial frequency speckle pattern could be observed. After few seconds this movement becomes less intense to the point that concentric low-spatial frequency contour fringes diverging from the interferogram center were discernible. When the process of heat deposition gets stationary the contour fringe pattern stops changing. In our experimental conditions, the time interval between sample illumination and thermal equilibrium was typically ~ 10 s. Figure 3(a) shows the two-wavelength speckle pattern describing the spherical-like wavefront generated by the thermal lens for a pump power of 1.76 W and an absorbed power of 0.76 W. Figure 3(b) shows the phase map after the four-stepping procedure and Figure 3(c) shows the resulting unwrapped phase. The three-dimensional wave-

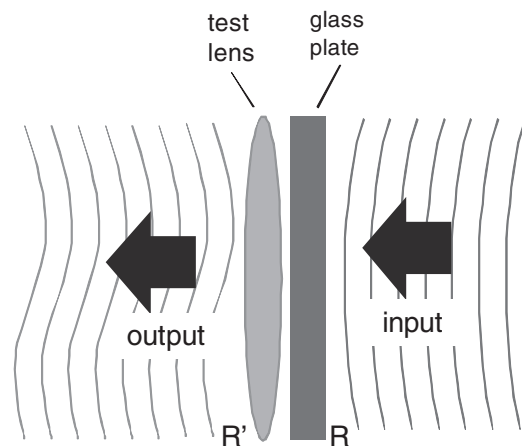


FIG. 4. Wavefront passing through the glass plate and the test lens.

front reconstruction is shown in Figure 3(d). With the help of this figure and of Eq. (2), the wavefront radius of curvature was determined to be $R_2 \approx 12.2$ cm. For a measured value of $x = 25.7$ mm from Eq. (7) the focal length of the induced lens is estimated to be $f_{\text{TL}} \approx 8.5$ cm. Figure 3 confirms the expected behavior of the sample submitted to a thermal lens effect: the maximum wavefront deformation seen in Figure 3(d) coincides with the region of maximal intensity of

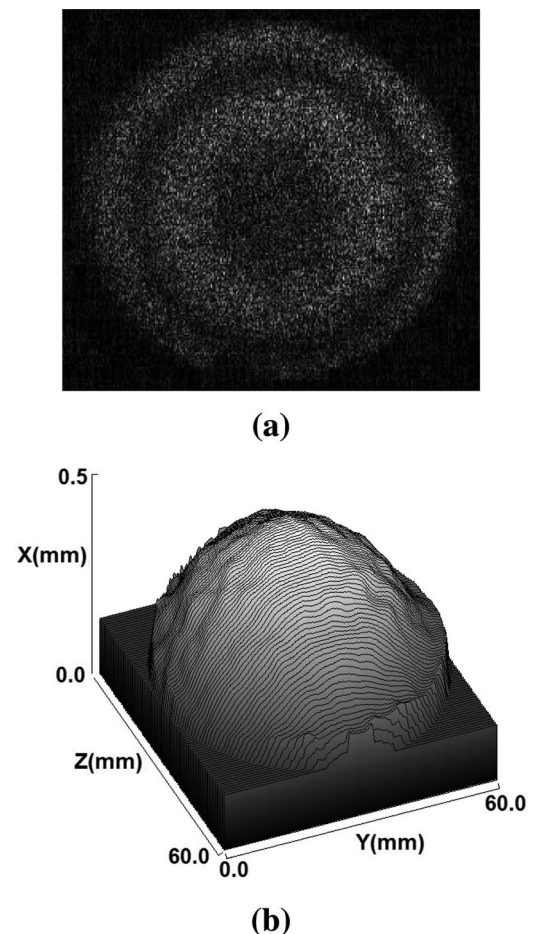


FIG. 5. Wavefront after passing through a spherical lens: (a) speckle pattern; (b) 3D reconstruction.

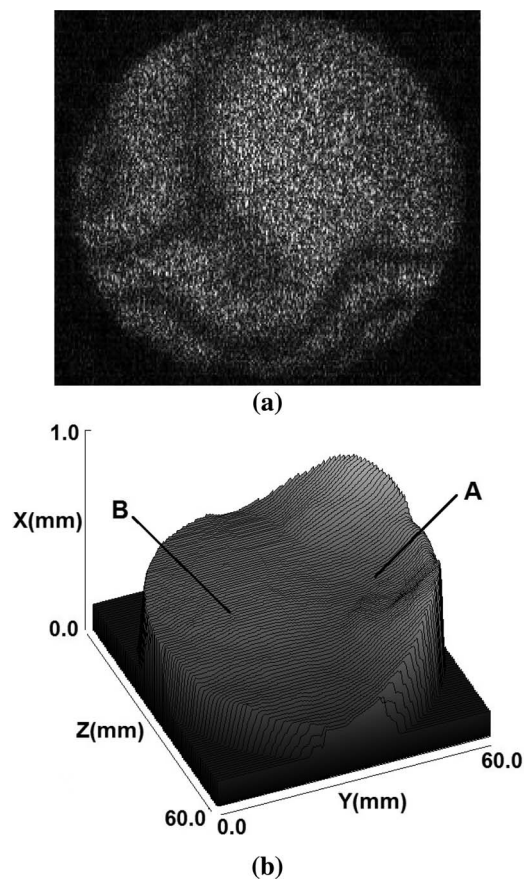


FIG. 6. Wavefront after passing through a progressive lens: (a) speckle pattern; (b) 3D reconstruction.

the pump beam. In the adjacent regions, as the beam intensity decreases, the wavefront deformation becomes smaller, thus assuming a spherical-like symmetry.

B. Measurement of wavefronts generated by passive phase elements

By using lenses with focal lengths $f_1 = 0.5$ cm and $f_2 = 20$ cm the diffusive plate was illuminated by a 60-mm diameter, nearly collimated beam. The residual wavefront was reconstructed by keeping the contour interval of $120 \mu\text{m}$ and performing the image acquisition and fringe evaluation procedures as described previously. The average radius of curvature of the reconstructed surface was measured to be $R' = -951 \pm 4$ mm. A 60-mm diameter, spherical lens with a 60-cm focal length was then positioned after the diffusive plate as shown in Figure 4 and the lasers were tuned to provide a contour interval of $140 \pm 1 \mu\text{m}$. The speckle image of the glass plate with the resulting two-wavelength interferogram and the 3D reconstruction of the wavefront after phase unwrapping are displayed in Figures 5(a) and 5(b), respectively. As expected for this kind of test lens, the wavefront generated by it has a spherical shape with a 1820 ± 9 mm radius of curvature. Through Eq. (8) the focal length of the test lens was calculated to be $f_L = 62.5 \pm 0.4$ cm, which is in good agreement with the nominal value of 60 cm. All the uncertainties were determined according to the procedure adopted

in Ref. 26. In order to test the performance of our setup in the analysis of more complex shapes with positive and negative slopes the wavefront generated by a progressive power lens (Alfalux Mid) was also measured. The contour interval was set to $120 \mu\text{m}$ and the resulting speckle pattern and the 3D wavefront reconstruction are displayed in Figures 6(a) and 6(b), respectively. Such a measurement is extremely useful for the evaluation of several types of geometrical aberrations. For the sake of qualitative evaluation, it can be seen from Figure 6(b) that the wavefront obtained through our DSPI technique presents some expected characteristics for this type of lens, evidenced by the regions surrounding points A and B. In the first, the resulting wavefront is concave, corresponding to a positive dioptric power of the progressive lens. In the latter, the wavefront is nearly flat, which corresponds to the region of least dioptric power.

V. CONCLUSION

The development and the performance of a two-wavelength wavefront sensor based on digital speckle pattern interferometry for induced lens phenomena and optical component analysis were demonstrated. The optical setup was conceived in order to enable both measurements without major changes in the optical setup. The whole-field nature of the technique provides information about the complete wavefront in single data acquisitions and allows both quantitative testing and real-time visual inspection.

By properly tuning the lasers, the measurement sensitivity and accuracy can be scaled according to the wavefront geometry and the testing requirements. With further progress in increasing the pixel density of the CCD and CMOS devices, digital whole-field interferometry is a promising technique for obtaining low-noise, high quality interference fringes, and high-spatial resolution measurements.

ACKNOWLEDGMENTS

This work was partially sponsored by Conselho Nacional de Desenvolvimento Científico e Tecnológico (CNPq) under Grant No. 477338/2009-7.

- ¹J. M. Geary, *Introduction to Wavefront Sensors* (SPIE, Bellingham, 1995).
- ²B. C. Platt and R. Shack, *J. Refract. Surg.* **17**, 573 (2001).
- ³M. Cui, *Opt. Lett.* **36**, 870 (2011).
- ⁴P. F. Almoró, G. Pedrini, P. N. Gundu, W. Osten, and S. G. Hanson, *Opt. Lasers Eng.* **49**, 252 (2011).
- ⁵P. F. Almoró and S. G. Hanson, *Appl. Opt.* **47**, 2979 (2008).
- ⁶D. Malacara, K. Creath, J. Schmit, and J. C. Wyant, in *Optical Shop Testing*, edited by D. Malacara (Wiley, New York, 2007), p. 435.
- ⁷J. A. Pomarico and R. D. Torroba, *Opt. Commun.* **141**, 1 (1997).
- ⁸R. A. Arizaga, J. A. Pomarico, and R. D. Torroba, *Opt. Commun.* **152**, 6 (1998).
- ⁹E. A. Barbosa and S. C. dos Santos, *Opt. Commun.* **281**, 1022 (2008).
- ¹⁰E. A. Barbosa, C. B. F. de Sousa, and W. M. Maffei, *Appl. Opt.* **48**, 5114 (2009).
- ¹¹U. Schnars and W. P. O. Jüptner, *Appl. Opt.* **33**, 4373 (1994).
- ¹²C. Wagner, W. Osten, and S. Seebacher, *Opt. Eng.* **39**, 7 (2000).
- ¹³I. Yamaguchi, S. Ohta, and J. Kato, *Opt. Lasers Eng.* **36**, 417 (2001).
- ¹⁴P. F. Almoró, G. Pedrini, A. Anand, W. Osten, and S. G. Hanson, *Opt. Lett.* **33**, 2041 (2008).
- ¹⁵J. E. Millerd and N. J. Brock, *Appl. Opt.* **36**, 2427 (1997).

- ¹⁶E. Hack, B. Frei, R. Kästle, and U. Sennhauser, *Appl. Opt.* **37**, 2591 (1998).
- ¹⁷E. A. Barbosa, *Appl. Phys. B* **80**, 345 (2005).
- ¹⁸P. Hariharan, B. F. Oreb, and T. Eiju, *Appl. Opt.* **26**, 2504 (1987).
- ¹⁹K. Creath, *Phase Measurement Techniques: Progress in Optics* (Elsevier, 1988), Vol. 26, p. 350.
- ²⁰T. Endo, Y. Yasuno, S. Makita, M. Itoh, and T. Yatagai, *Opt. Express* **13**, 695 (2005).
- ²¹B. Gutmann and H. Weber, *Appl. Opt.* **38**, 5577 (1999).
- ²²G. Pedrini, H. J. Tiziani, and M. E. Gusev, *Appl. Opt.* **39**, 246 (2000).
- ²³E. DelRe and M. Segev, in *Self-focusing: Past and Present: Fundamentals and Prospects*, edited by R. W. Boyd, S. G. Lukishova, Y. R. Shen (Springer, Berlin, 2010), p. 547.
- ²⁴M. R. R. Gesualdi, M. Muramatsu, and E. A. Barbosa, *Opt. Commun.* **281**, 5739 (2008).
- ²⁵J. T. Verdeyen, *Laser Electronics* (Prentice Hall, Englewood Cliffs, NJ, 2008).
- ²⁶E. A. Barbosa, R. Verzini, and J. F. Carvalho, *Opt. Commun.* **263**, 189 (2006).